A Thermal Lattice Boltzmann Model for Flows with Viscous Heat Dissipation

Hao-Chueh Mai[1], Kuen-Hau Lin[1], Cheng-Hsiu Yang[1] and Chao-An Lin[1,2]

Abstract: A thermal BGK lattice Boltzmann model for flows with viscous heat dissipation is proposed. In this model, the temperature is solved by a separate thermal distribution function, where the equilibrium distribution function is similar to its hydrodynamic counterpart, except that the leading quantity is temperature. The viscous dissipation rate is obtained by computing the second-order moments of non-equilibrium distribution function, which avoids the discretization of the complex gradient term, and can be easily implemented. The proposed thermal lattice Boltzmann model is scrutinized by computing two-dimensional thermal Poiseuille flow, thermal Couette flow, natural convection in a square cavity, and three-dimensional thermal Poiseuille flow in a square duct. Numerical simulations indicate that the second order accurate LBM scheme is not degraded by the present thermal BGK lattice Boltzmann model.

Keywords: Thermal lattice Boltzmann model, viscous heat dissipation, BGK model, natural convection, second order accuracy.

1 Introduction

Explicit, easy to implement, and natural to parallelize are the major advantages of Lattice Boltzmann method (LBM), which has been successfully applied to various isothermal hydrodynamic and engineering problems [Yu, Mei, Luo, and Shyy (2003); Chen, Chang, and Sun (2007); Han, Feng, and Owen (2007); Mishra, Paik, and Atluri (2009)]. However, its direct extension to the thermal flows is not straightforward, because of the numerical instability for thermal models [McNamara, Garcia, and Alder (1995)]. In general, the thermal lattice Boltzmann model (TLBM) can be categorized into two types [He, Chen, and Doolen (1998)]. The first one is the multi-speed approach and the second one is the passive scalar model. The multi-

---

[1] Department of Power Mechanical Engineering, National Tsing Hua University, Hsinchu 30013, Taiwan.

[2] Corresponding author, calin@pme.nthu.edu.tw

speed approach is a straightforward extension of the lattice Boltzmann isothermal models in which only the density distribution function is used. On the other hand, the passive scalar approach utilizes the fact that the macroscopic temperature satisfies the same evolution equation as a passive scalar, which is advected by the flow velocity but does not affect the flow fields. The major advantage of the passive scalar model over the multi-speed approach is the enhancement of the numerical stability and is thus commonly adopted.

In the passive scalar thermal lattice Boltzmann models, a separate distribution function is used to solve for the temperature distribution and the distribution function may be similar to its hydrodynamic counterpart[Shi, Zhao, and Guo (2004); Li, He, Wang, and Tang (2008)] or different [He, Chen, and Doolen (1998); Peng, Shu, and Chew (2003); Tang, Tao, and He (2005)]. For example, a double-distribution-function model was proposed by He, Chen, and Doolen (1998). This model has a better numerical stability than the multispeed approach, and the viscous heat dissipation and compression work done by the pressure can be solved implicitly. However, the major drawback of this thermal model is the complex discretization to obtain the viscous dissipation rate, which includes a complicated gradient term involving temporal and spatial derivatives of the macroscopic flow variables. Another thermal model with viscous dissipation rate was proposed by Shi, Zhao, and Guo (2004), however complex discretization of the velocity gradient is still needed.

To model the incompressible thermal flows without viscous heat dissipation, Peng, Shu, and Chew (2003) proposed a simplified thermal lattice Boltzmann model, where the complicated gradient term in this model is neglected. However, Li, He, Wang, and Tang (2008) indicated that this direct neglecting of the gradient term may affect the original conduction equation. To overcome this, Li, He, Wang, and Tang (2008) proposed an improved thermal lattice Boltzmann model for flows without viscous heat dissipation and compression work. Based on the work of He, Chen, and Doolen (1998), Tian, Zuo, Liu, Liu, Guo, and Zheng (2006) proposed a simpler implementation of the viscous dissipation term. However, the second order accuracy of the LBM model is not satisfied.

In this paper, a thermal lattice Boltzmann model with viscous heat dissipation in the incompressible limit is presented, where a separate distribution function is adopted to solve for the temperature field. The thermal lattice Boltzmann equation is modeled through the convection-diffusion equation with a source term. Here, the thermal equilibrium distribution function is similar to its hydrodynamic BGK LBM counterpart, except that the leading quantity is temperature. Also, to avoid discretizing the gradient term of the strain rate tensor, the viscous dissipation rate can be obtained by computing the second-order moments of non-equilibrium distribution function. This greatly simplifies the evaluation of the viscous dissipation

term. Novel hydrodynamic and thermal boundary conditions are adopted in the present study. The validity and accuracy of this new thermal lattice Boltzmann model is scrutinized by computing two-dimensional thermal Poiseuille flow, thermal Couette flow, and natural convection in a square cavity. Moreover, to validate its consistent formulation to three-dimensional problems, a 3-D thermal Poiseuille flow in a square duct is also simulated. The results show that the proposed thermal lattice Boltzmann model can be implemented easily, and the second order accuracy is also satisfied.

2 Thermal lattice Boltzmann models

As indicated earlier, a separate distribution function is adopted to solve for the temperature field, where the thermal lattice Boltzmann equation is modeled through the convection-diffusion equation with a source term [Deng, Shi, and Wang (2005)]. Here, the temperature is regarded as a scalar quantity, and the viscous dissipation term is treated as source term.

The governing equations for the thermal energy distribution model could be expressed as,

$$f_i(\vec{x} + \vec{e}_i \triangle t, t + \triangle t) = f_i(\vec{x}, t) - \frac{1}{\tau_f}[f_i(\vec{x}, t) - f_i^{eq}(\vec{x}, t)] \tag{1}$$

$$g_i(\vec{x} + \vec{e}_i \triangle t, t + \triangle t) = g_i(\vec{x}, t) - \frac{1}{\tau_g}[g_i(\vec{x}, t) - g_i^{eq}(\vec{x}, t)] + \triangle t F_i + \frac{1}{2}(\triangle t)^2 \frac{\partial F_i}{\partial t} \tag{2}$$

where f_i and g_i are the particle density and temperature energy distribution functions along the particle velocity direction $\vec{e}_i$, respectively. C_s is the sound speed which depends on the lattice model used. τ_f and τ_g are the dimensionless relaxation times that control the rates approaching equilibrium. The time derivative of the force is discretized using the simple forward difference scheme as,

$$\frac{\partial F_i(\vec{x}, t)}{\partial t} = [F_i(\vec{x}, t) - F_i(\vec{x}, t - \triangle t)]/\triangle t \tag{3}$$

The term F_i represents the effect of viscous heating and F_i can be determined by [Deng, Shi, and Wang (2005)],

$$F_i = \omega_i \frac{\Phi}{c_v}[1 + \frac{\vec{e}_i \cdot \vec{u}}{C_s^2} \frac{\tau_g - 1/2}{\tau_g}] \tag{4}$$

c_v is the specific heat at constant volume. The viscous heating term Φ can be expressed as follows:

$$\Phi = 2\mu S_{\alpha\beta} S_{\alpha\beta} - \frac{2\mu}{3}(\triangledown \cdot \vec{u})^2 \tag{5}$$

where the strain rate tensor $S_{\alpha\beta}$ can be defined as:

$$S_{\alpha\beta} = \frac{1}{2}(\frac{\partial u_\alpha}{\partial x_\beta} + \frac{\partial u_\beta}{\partial x_\alpha})$$

$S_{\alpha\beta}$ can be expressed by the momentum fluxes $Q_{\alpha\beta}$, which can be obtained by computing the second-order moments of non-euilibrium distribution function [Hou, Sterling, Chen, and Doolen (1996)].

$$S_{\alpha\beta} = \frac{-1}{2\rho C_s^2 \tau} Q_{\alpha\beta}, Q_{\alpha\beta} = \sum_i e_{i\alpha} e_{i\beta}(f_i - f_i^{eq}) \tag{6}$$

The macroscopic variables can be evaluated as the moment of the distribution function:

$$\sum_i f_i^{eq} = \rho \tag{7}$$

$$\sum_i \vec{e}_{i\alpha} f_i^{eq} = \rho \vec{u} \tag{8}$$

$$\sum_i g_i^{eq} = \rho T \tag{9}$$

$$\sum_i e_{i\alpha} g_i^{eq} = \rho u_\alpha T \tag{10}$$

$$\sum_i e_{i\alpha} e_{i\beta} g_i^{eq} = \rho u_\alpha u_\beta T + C_s^2 \rho T \delta_{ij} \tag{11}$$

For the present 2D and 3D applications, D2Q9 and D3Q19 models are adopted. The equilibrium density distribution functions and equilibrium temperature energy distribution functions for these two models are

$$f_i^{eq} = \omega_i \rho [1 + \frac{3\vec{e}_i \cdot \vec{u}}{C^2} + \frac{9(\vec{e}_i \cdot \vec{u})^2}{2C^4} - \frac{3\vec{u} \cdot \vec{u}}{2C^2}] \tag{12}$$

$$g_i^{eq} = \omega_i \rho T [1 + \frac{3\vec{e}_i \cdot \vec{u}}{C^2} + \frac{9(\vec{e}_i \cdot \vec{u})^2}{2C^4} - \frac{3\vec{u} \cdot \vec{u}}{2C^2}] \tag{13}$$

where the weighting factors ω_i are $\omega_0 = 4/9$, $\omega_{i=1\sim4} = 1/9$, $\omega_{i=5\sim8} = 1/36$, and $\omega_0 = 1/3$, $\omega_{i=1\sim6} = 1/18$, $\omega_{i=7\sim18} = 1/36$ for D2Q9 and D3Q19 models, respectively. $C = \triangle x/\triangle t$ is the lattice speed, where $\triangle x$ and $\triangle t$ are the lattice width and time step, respectively.

The macroscopic temperature equation can be derived through the Chapman-Enskog procedure. Details of the derivation are given in Appendix A.

$$\frac{\partial T}{\partial t} + \nabla \cdot (\vec{u}T) = \frac{k}{\rho c_v} \nabla^2 T + \frac{\Phi}{\rho c_v} \tag{14}$$

The corresponding kinematic viscosity and thermal conductivity are calculated by $v = (\tau_f - 0.5)C_s^2 \triangle t$ and $k = \rho c_v (\tau_g - 0.5)C_s^2 \triangle t$, where $C_s = \sqrt{RT} = C/\sqrt{3}$ is the speed of sound.

The present study is concerned with laminar flow simulations. However, for turbulent flow simulations, the relaxation times should be modified [Teixeira (1998)] to account for the eddy viscosity from the turbulence models [Hwang and Lin (1999, 2000)].

3 Boundary conditions

3.1 *Hydrodynamic boundary conditions*

Boundary condition proposed in [Chang, Liu, and Lin (2009)] and [Ho, Chang, Lin, and Lin (2009)] is employed to determine the unknown particle density distribution functions along the boundary, which are expressed as a combination of the local known value and a corrector,

$$f_p(\vec{x}, \vec{e}_p, t) = f_p^*(\vec{x}, \vec{e}_p, t) + \frac{\omega_p}{C}\vec{e}_p \cdot \vec{Q} \qquad (15)$$

where $\vec{Q}$ is the corrector to enforce the required momentum. For instance, consider a node at the top boundary as shown in Fig. 1, where the unknown density distribution functions are f_4, f_7 and, f_8, i.e. $f_4 = f_4^* - \omega_4 Q_y$, $f_7 = f_7^* - \omega_7(Q_x + Q_y)$, and $f_8 = f_8^* + \omega_8(Q_x - Q_y)$. Therefore, the macroscopic velocity and density at the node using Eqs. 7 and 8, in conjunction with Eq. 15, can be expressed as,

$$
\begin{aligned}
\rho &= f_0 + f_1 + f_2 + f_3 + (f_4^* - \omega_4 Q_y) + f_5 + f_6 \\
&+ [f_7^* - \omega_7(Q_x + Q_y)] + [f_8^* + \omega_8(Q_x - Q_y)] \qquad (16) \\
\rho u &= f_1 + f_5 + [f_8^* + \omega_8(Q_x - Q_y)] - f_3 - f_6 - [f_7^* - \omega_7(Q_x + Q_y)] \qquad (17) \\
\rho v &= f_2 + f_5 + f_6 - (f_4^* - \omega_4 Q_y) \\
&- [f_7^* - \omega_7(Q_x + Q_y)] - [f_8^* + \omega_8(Q_x - Q_y)] \qquad (18)
\end{aligned}
$$

If velocities u and v are known at the boundary, Eq. 16 to 18 can be used to solve for ρ, Q_x, and Q_y, and then f_4, f_7, and f_8 are obtained. For simplicity, $f_p^*(\vec{x}, \vec{e}_p, t) = f_p(\vec{x}, -\vec{e}_p, t)$ are adopted. The explicit forms of the unknown particle

density distribution functions are shown as below.

$$\rho = \frac{1}{1+v}[f_0 + f_1 + f_3 + 2(f_2 + f_5 + f_6)]$$

$$f_4 = f_2 - \frac{2}{3}\rho v$$

$$f_7 = f_5 + \frac{1}{2}(f_1 - f_3) - \frac{1}{2}\rho u - \frac{1}{6}\rho v$$

$$f_8 = f_6 - \frac{1}{2}(f_1 - f_3) + \frac{1}{2}\rho u - \frac{1}{6}\rho v \tag{19}$$

For boundary does not coincide with the lattices, special treatment has to be taken to model the solid-fluid boundary, such as those in [Chen, Lin, and Lin (2007)] and [Yang, Chang, and Lin (2009)], which are based on the immersed boundary methods in [Su, Lai, and Lin (2007)] and [Liao, Chang, Lin, and McDonough (2010)], respectively.
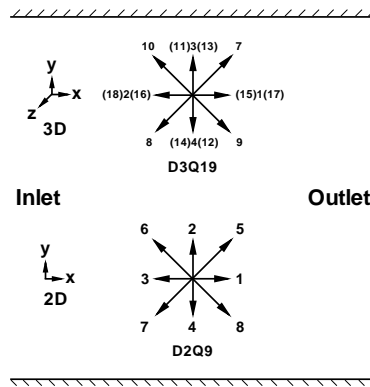
Figure 1: The 2D and 3D models.

3.2 Thermal boundary conditions

Here, similar to its hydrodynamic counterpart, a consistent thermal boundary condition is introduced [Liu, Lin, Mai, and Lin (2010)]. The unknown particle energy distribution function at the plane boundary is assumed to be,

$$g_p(\vec{x}, \vec{e}_p, t) = g_p^*(\vec{x}, \vec{e}_p, t) + \omega_p G_c \tag{20}$$

where G_c is the correction to enforce the internal energy.

For instance, consider a node at the top boundary as shown in Fig. 1, where the unknown particle energy distribution functions are (g_4, g_7, g_8) and $(g_4, g_8, g_9, g_{12}, g_{14})$, respectively for D2Q9 and D3Q19 models. Therefore, the internal energy density at the node using Eq. 9, in conjunction with Eq. 20, can be expressed as,

For the D2Q9 model,

$$
\begin{aligned}
\rho T &= g_0 + g_1 + g_2 + g_3 + [g_4^* + \omega_4 G_c] + g_5 + g_6 \\
&+ [g_7^* + \omega_7 G_c] + [g_8^* + \omega_8 G_c] \tag{21} \\
\rho T^* &= g_0 + g_1 + g_2 + g_3 + g_4^* + + g_5 + g_6 + g_7^* + g_8^* \tag{22} \\
G_c &= \frac{\rho T - \rho T^*}{\omega_4 + \omega_7 + \omega_8} \tag{23}
\end{aligned}
$$

For the D3Q19 model,

$$
\begin{aligned}
\rho T &= g_0 + g_1 + g_2 + g_3 + [g_4^* + \omega_4 G_c] + g_5 + g_6 + g_7 \\
&+ [g_8^* + \omega_8 G_c] + [g_9^* + \omega_9 G_c] + g_{10} + g_{11} \\
&+ [g_{12}^* + \omega_{12} G_c] + g_{13} + [g_{14}^* + \alpha_{14} G_c] \\
&+ g_{15} + g_{16} + g_{17} + g_{18} \tag{24} \\
\rho T^* &= g_0 + g_1 + g_2 + g_3 + g_4^* + g_5 + g_6 + g_7 + g_8^* + g_9^* + g_{10} \\
&+ g_{11} + g_{12}^* + g_{13} + g_{14}^* \tag{25} \\
G_c &= \frac{\rho T - \rho T^*}{\omega_4 + \omega_8 + \omega_9 + \omega_{12} + \omega_{14}} \tag{26}
\end{aligned}
$$

The temperature T is known at the boundary, hence (g_4, g_7, g_8) and $(g_4, g_8, g_9, g_{12}, g_{14})$ are obtained for D2Q9 and D3Q19 models. The explicit forms of the unknown particle energy distribution functions are shown below.

For the D2Q9 model,

$$
\begin{aligned}
T^* &= \frac{1}{\rho}(g_0 + g_1 + g_2 + g_3 + g_4^* + g_5 + g_6 + g_7^* + g_8^*) \\
g_4 &= g_4^* + \frac{2}{3}\rho(T - T^*) \\
g_7 &= g_7^* + \frac{1}{6}\rho(T - T^*) \\
g_8 &= g_8^* + \frac{1}{6}\rho(T - T^*) \tag{27}
\end{aligned}
$$

For the D3Q19 model,

$$
\begin{aligned}
T^* &= \frac{1}{\rho}(g_0 + g_1 + g_2 + g_3 + g_4^* + g_5 + g_6 + g_7 + g_8^* + g_9^* + g_{10} \\
&+ g_{11} + g_{12}^* + g_{13} + g_{14}^* + g_{15} + g_{16} + g_{17} + g_{18}) \\
g_4 &= g_4^* + \frac{1}{3}\rho(T - T^*) \\
g_8 &= g_8^* + \frac{1}{6}\rho(T - T^*) \\
g_9 &= g_9^* + \frac{1}{6}\rho(T - T^*) \\
g_{12} &= g_{12}^* + \frac{1}{6}\rho(T - T^*) \\
g_{14} &= g_{14}^* + \frac{1}{6}\rho(T - T^*)
\end{aligned}
\tag{28}
$$

For simplicity, the formulation of $g_p^* = g_p^{eq}(\vec{x}, \vec{e}_p, t)$ is adopted here. Other forms have been explored such as, $g_p^*(\vec{x}, \vec{e}_p, t) = g_p(\vec{x}, -\vec{e}_p, t)$ and $g_p^*(\vec{x}, \vec{e}_p, t) = g_p(\vec{x}, \vec{e}_p, t - \triangle t)$, and influences were found to be marginal on the predicted results as shown in Liu, Lin, Mai, and Lin (2010).

4 Numerical results

4.1 2-D thermal Poiseuille flow

Fully developed flow in a channel is a typical case to examine the accuracy of boundary conditions. Here, the two-dimensional Poiseuille flow with constant wall temperature T_t is considered. The Reynolds number is defined as $Re = U_0 H / v$ in a channel of height H, and U_0 is the maximum velocity. The effect of viscous heat dissipation is controlled by the Prandtl number $Pr = v/\chi$. The pressure gradient is set as $\partial p / \partial x = -8\rho v U_0 / H^2$. The analytical solution for the temperature field and the maximum relative error are defined as,

$$
T_{exact}(y) = T_t + \frac{1}{3}PrU_0^2\left[1 - (\frac{2y}{H} - 1)^4\right]
\tag{29}
$$

$$
Err_{max} = max(\frac{\sqrt{(T - T_{exact})^2}}{T_t})
\tag{30}
$$

Velocity boundary conditions and the proposed Dirichlet thermal boundary conditions are applied along the channel walls. Mixed pressure velocity boundary conditions and periodic thermal boundary conditions are used at the channel inlet and outlet. Fig. 2 shows the temperature profiles in comparison with the analytic
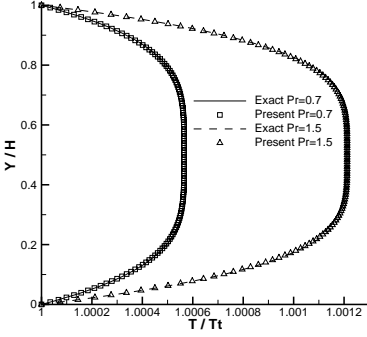
Figure 2: The temperature profiles of 2-D Poiseuille flow with $Re = 10$, 5×129 grid, and $\tau_f = 1.1$.
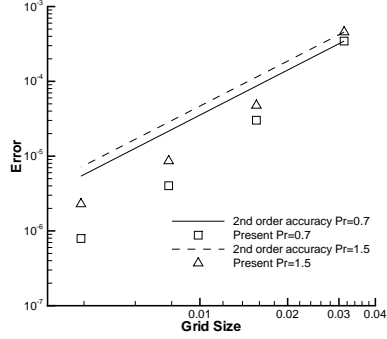
Figure 3: Maximum predicted temperature relative errors of 2-D Poiseuille flow.

solution for different Prandtl numbers. Five different lattice densities in the *y* direction are adopted, (21, 41, 81, 161, and 321). Fig. 3 shows that the predicted results are slightly higher than second-order accurate for the Prandtl numbers investigated. This is due to the periodic boundary conditions adopted for the energy equation.

4.2 2-D thermal Couette flow

Next, attention is directed to the two-dimensional thermal Couette flow. This is to examine the validity of the proposed thermal boundary conditions at moving wall. Here, the channel top wall is moving at a constant velocity U_t with a higher constant temperature T_t, and the bottom wall is stationary with a lower constant temperature T_b. The Reynolds number is defined as $Re = U_t H / \nu$ in a channel of height H. The major control parameters are the Prandtl number and the Eckert number $Ec = U_t^2 / (C_v \triangle T)$, where $\triangle T$ is the temperature difference between the hot and cold walls. The effect of viscous heat dissipation is controlled by the Brinkman number $Br = PrEc$. The analytical solution for this temperature field is expressed as,

$$T_{exact}(y) = T_b + \frac{y}{H}[1 + 0.5Br(1 - \frac{y}{H})]\triangle T \tag{31}$$

Velocity boundary conditions and the proposed Dirichlet thermal boundary conditions are applied along the channel walls, and the periodic boundary condition is applied at the inlet and outlet. Fig. 4 shows the temperature profiles in comparison with the analytic solution for different Brinkman numbers while the Prandtl
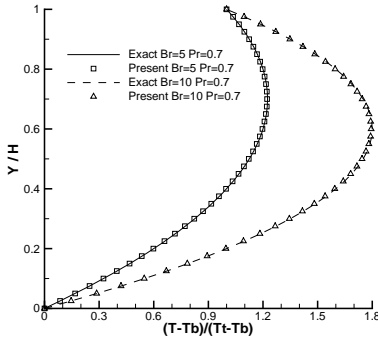
Figure 4: The temperature profiles of 2-D Couette flow with $Re = 10$, 5×41 grid, and $\tau_f = 0.9$.
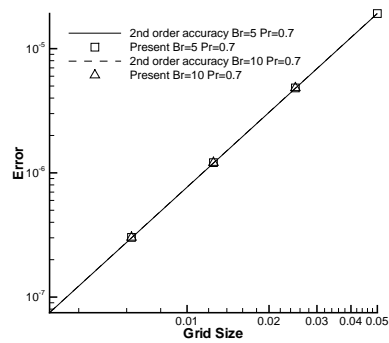
Figure 5: Maximum predicted temperature relative errors of 2-D Couette flow.

number is fixed. Five different lattice densities in the *y* direction are adopted, (21, 41, 81, 161, and 321), to determine the convergence rate in space. To examine the convergence, Eq. 30 is also used to determine the maximum relative error using different lattices. Fig. 5 shows the predicted results and the second-order accuracy is achieved.

4.3 3-D thermal Poiseuille flow in a square duct

Here, the capability of the proposed thermal boundary conditions to model 3-D problems is examined. A pressure driven 3-D square duct flow with constant wall temperatures is simulated by the D3Q19 model. Mixed pressure velocity boundary conditions and periodic thermal boundary conditions are applied at the duct inlet and outlet boundaries. No-slip condition and Dirichlet thermal boundary conditions are imposed along the bounding walls. The corner treatment is similar to its 2D flow counterpart and is not repeated here. The size of the square duct is $0 \leq x \leq L$, $-H \leq y \leq H$ and $-H \leq z \leq H$, where L and H are duct length and half of the duct height, with x being the flow direction. The lattice sizes are $N_x \times N_y \times N_z$:$5 \times 33 \times 33$. The adopted Reynolds number is 1 and the Prandtl number is 0.7. The corresponding τ_f and τ_g are both 0.9.

Figs. 6 and 7 show the streamlines and isotherms within the square duct. The velocity and temperature profiles along the vertical wall bisector at $x/L = 0.5$ can be referred to Figs. 8 and 9. It is clear that the presence of the viscous dissipation increases the temperature levels within the square duct, which is observed by the
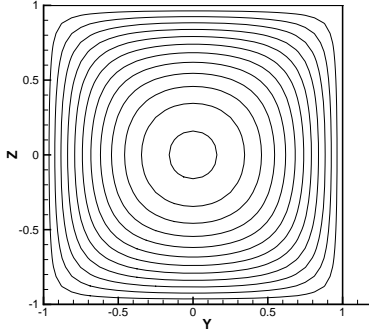
Figure 6: The streamline of 3-D Poiseuille flow in a square cavity.
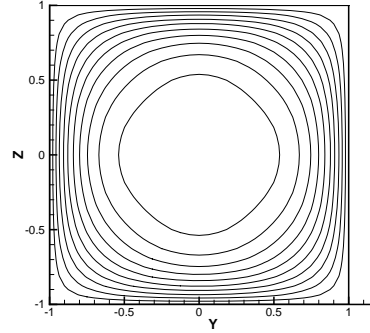
Figure 7: The isotherm of 3-D Poiseuille flow in a square cavity.

elevated level of temperature gradient compared to its hydrodynamic counterpart at the near wall region. Here, the flow is driven by a constant pressure gradient. However, for the temperature equation, the viscous dissipation is not uniform and depends on the velocity gradient, which is higher at the near wall region. This difference is reflected in the different distributions of the predicted velocity and temperature profiles.

4.4 2-D natural convection in a square cavity

Natural convection problems within confined enclosure were commonly investigated [Davis (1983); Nicolas, Bermudez, and Baez (2009); Anguiano-Orozco and Avila (2009); Liu, Lin, Mai, and Lin (2010)]. Here, focus is directed to the natural convection in a square cavity, where the flow is driven by the buoyancy force due to the differential temperature of the sidewalls. The left wall is at the higher uniform temperature T_l and the right wall is at the lower uniform temperature T_r. Both the top and bottom walls are adiabatic. With the Boussinesq approximation, the buoyancy term is assumed to depend linearly on the temperature as,

$$\rho \vec{G} = \rho \beta \mathbf{g}(T - T_m)\vec{j} \tag{32}$$

where β is the thermal expansion coefficient, $\mathbf{g}$ is the acceleration due to gravity, $T_m = (T_l + T_r)/2$ is the average temperature, and $\vec{j}$ is the vertical direction opposite to that of gravity. To account for this Buoyancy induced force, an extra forcing
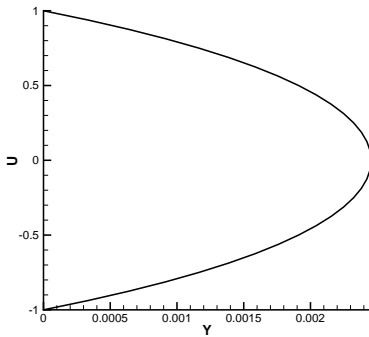
Figure 8: The velocity profiles of 3-D Poiseuille flow in a square duct along the vertical wall bisectors at $x/L = 0.5$..
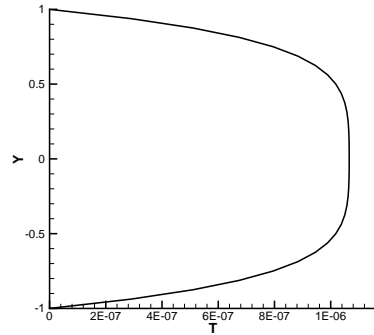
Figure 9: The temperature profiles of 3-D Poiseuille flow in a square duct along the vertical wall bisectors at $x/L = 0.5$..

term F_i is added to Eq. 1 and is expressed as [He, Zou, Luo, and Dembo (1997)],

$$F_i = 3\omega_i \frac{\vec{G} \cdot \vec{e}_i}{C} \tag{33}$$

The major control parameter is the Rayleigh number $Ra = \beta \mathbf{g} \triangle T H^3 Pr/v^2$ associated with the heat transfer within the fluid, where H is the height or width of the cavity. For the Rayleigh number investigated, the influence of the viscous dissipation is negligible. However, the present section serves to examine the applicability of the present thermal model under such conditions by comparing with previous predicted results [Davis (1983) and Liu, Lin, Mai, and Lin (2010)] using different methodologies.

The domain is covered by a lattice sizes of 101×101, 151×151, 201×201, 201×201, and 251×251, respectively for $Ra = 10^3, 10^4, 10^5$ and 10^6. Table 1 shows the numerical results of the maximum horizontal velocity on the vertical midplane of the cavity, u_{max} , and its location y, the maximum vertical velocity on the horizontal midplane of the cavity, v_{max}, and its location x, and the average Nusselt number $\overline{Nu}$ for Rayleigh numbers conducted at $Ra = 10^3, 10^4, 10^5$ and 10^6. Note that the velocity shown in the table is normalized by the reference velocity of χ/H. Figs. 10, and 11 show the streamlines, and isotherms at different Rayleigh numbers, respectively. The simulated results are contrasted with the solutions of Davis (1983) and Liu, Lin, Mai, and Lin (2010) using different methodologies and

Table 1: Predicted results compared with the solutions of Davis (1983) and Liu, Lin, Mai, and Lin (2010) for 2-D natural convection in a square cavity.

Ra		10^3	10^4	10^5	10^6
u_{max}	**Davis**	3.649	16.178	34.73	64.63
	Liu et al.	3.649	16.148	34.485	63.421
	present	3.648	16.138	34.459	63.413
y	**Davis**	0.813	0.823	0.855	0.850
	Liu et al.	0.810	0.820	0.855	0.848
	present	0.810	0.820	0.855	0.848
v_{max}	**Davis**	3.697	19.617	68.590	219.360
	Liu et al.	3.697	19.608	68.563	219.699
	present	3.697	19.602	68.551	219.708
x	**Davis**	0.178	0.119	0.066	0.0379
	Liu et al.	0.180	0.120	0.065	0.036
	present	0.180	0.120	0.065	0.036
$\overline{\overline{Nu}}$	**Davis**	1.118	2.243	4.519	8.800
	Liu et al.	1.115	2.230	4.488	8.747
	present	1.116	2.230	4.488	8.745

the agreements are satisfactory, as shown in Table 1.

5   Conclusion

A thermal BGK lattice Boltzmann model for flows with viscous heat dissipation is proposed, where a separate distribution function is adopted to solve for the temperature field. The thermal lattice Boltzmann equation is modeled through the convection-diffusion equation with a viscous dissipation source term, and the temperature is regarded as a scalar quantity. Proposed thermal equilibrium distribution function is similar to its hydrodynamic counterpart, except that the leading quantity is temperature. The viscous dissipation rate is obtained by computing the second-order moments of non-equilibrium distribution function, which avoids the discretization of the complex gradient term, and can be easily implemented. The proposed thermal lattice Boltzmann model is scrutinized by computing two-dimensional thermal Poiseuille flow, thermal Couette flow, natural convection in a square cavity, and three-dimensional thermal Poiseuille flow in a square duct. Numerical simulations indicate that the second order accurate LBM scheme is not degraded by the present thermal BGK lattice Boltzmann model. Also, the pre-

(a) Ra=10³ (b) Ra=10⁴ (c) Ra=10⁵ (d) Ra=10⁶
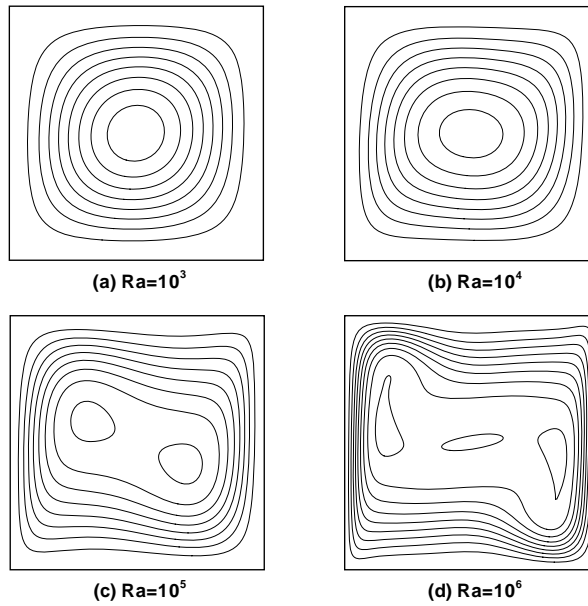
Figure 10: The streamline profiles of 2-D natural convection in a square cavity.

(a) Ra=10³ (b) Ra=10⁴ (c) Ra=10⁵ (d) Ra=10⁶
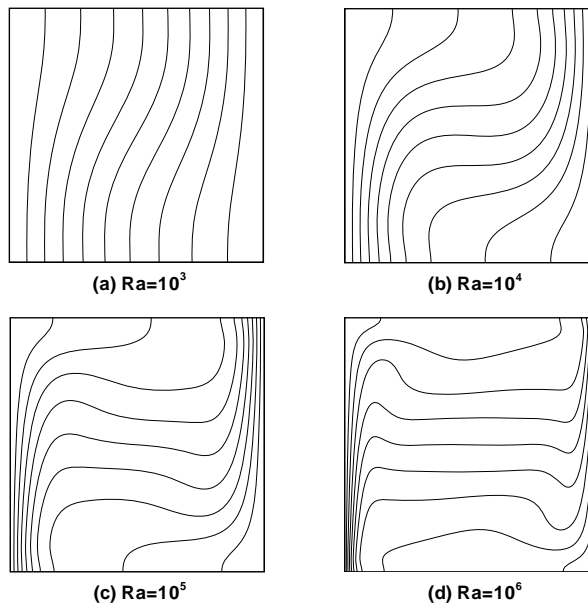
Figure 11: The isotherm profiles of 2-D natural convection in a square cavity.

dicted natural convection results compare favorably with the existing benchmark solutions.

6 Acknowledgments

References

Anguiano-Orozco, G.; Avila, R. (2009): Vortex Ring Formation within a Spherical Container with Natural Convection. *CMES: Computer Modeling in Engineering & Sciences*, vol. 49, no. 3, pp. 217–253.

Chang, C.; Liu, C. H.; Lin, C. A. (2009): Boundary conditions for lattice Boltzmann simulations with complex geometry flows. *Computers & Mathematics with Applications*, vol. 58, no. 5, pp. 940–949.

Chen, C. K.; Chang, S. C.; Sun, S. Y. (2007): Lattice Boltzmann method simulation of channel flow with square pillars inside by the field synergy principle. *CMES: Computer Modeling in Engineering & Sciences*, vol. 22, no. 3, pp. 203–215.

Chen, D. J.; Lin, K. H.; Lin, C. A. (2007): Immersed boundary method based lattice Boltzmann method to simulate 2D and 3D complex geometry flows. *International Journal of Modern Physics C*, vol. 18, no. 4, pp. 585–594.

Davis, G. D. (1983): Natural convection of air in a square cavity: a bench mark numerical solution. *Int. J. Numer. Methods Fluids*, vol. 3, pp. 249–264.

Deng, B.; Shi, B. C.; Wang, G. C. (2005): A new lattice Bhatnagar-Gross-Krook model for the convection-diffusion equation with a source term. *Chin. Phys. Lett.*, vol. 22, pp. 267–270.

Han, K.; Feng, Y. T.; Owen, D. R. J. (2007): Numerical simulations of irregular particle transport in turbulent flows using coupled LBM-DEM. *CMES: Computer Modeling in Engineering & Sciences*, vol. 18, no. 2, pp. 87–100.

He, X.; Chen, S.; Doolen, G. D. (1998): A novel thermal model for the lattice Boltzmann method in incompressible limit. *J. Comput. Phys.*, vol. 146, pp. 282–300.

He, X. Y.; Zou, Q. S.; Luo, L. S.; Dembo, M. (1997): Analytic solution of simple flows and analysis of nonslip boundary conditions for the lattice Boltzmann BGK model. *J. Stat. Phys.*, vol. 87, pp. 115–136.

Ho, C. F.; Chang, C.; Lin, K. H.; Lin, C. A. (2009): Consistent boundary conditions for 2D and 3D lattice Boltzmann simulations. *CMES: Computer Modeling in Engineering & Sciences*, vol. 44, no. 2, pp. 137–155.

Hou, S.; Sterling, J.; Chen, S.; Doolen, G. D. (1996): A lattice Boltzmann subgrid model for high Reynolds number flows. *Pattern formation and lattice gas automata. In: Lawniczak AT, Kapral R, editors Pattern formation and lattice gas automata. Fields Inst Commu*, vol. 6, pp. 151–166.

Hwang, C. B.; Lin, C. A. (1999): A low Reynolds number two-equation k_θ-$\tilde{\varepsilon}_\theta$ model to predict thermal fields. *International Journal of Heat and Mass Transfer*, vol. 42, no. 17, pp. 3217–3230.

Hwang, C. B.; Lin, C. A. (2000): Low-Reynolds number k-$\tilde{\varepsilon}$ modelling of flows with transpiration. *International Journal of Numerical Methods in Fluids*, vol. 32, no. 5, pp. 495–514.

Li, Q.; He, Y. L.; Wang, Y.; Tang, G. H. (2008): An improved thermal lattice Boltzmann model for flows without viscous heat dissipation and compression work. *Int. J. Mod. Phys. C*, vol. 19, pp. 125–150.

Liao, C. C.; Chang, Y. W.; Lin, C. A.; McDonough, J. M. (2010): Simulating flows with moving rigid boundary using immersed-boundary method. *Computers & Fluids*, vol. 39, no. 1, pp. 152–167.

Liu, C. H.; Lin, K. H.; Mai, H. C.; Lin, C. A. (2010): Thermal boundary conditions for thermal Lattice Boltzmann simulations. *Computers & Mathematics with Applications*, vol. 59, no. 7, pp. 2178–2193.

McNamara, G. R.; Garcia, A. L.; Alder, B. J. (1995): Stabilization of thermal lattice Boltzmann models. *J. Stat. Phys.*, vol. 81, pp. 395–408.

Mishra, S. K.; Paik, J. K.; Atluri, S. N. (2009): Modeling of the Inhibition-Mechanism Triggered by 'Smartly' Sensed Interfacial Stress Corrosion and Cracking. *CMES: Computer Modeling in Engineering & Sciences*, vol. 50, no. 1, pp. 67–96.

Nicolas, A.; Bermudez, B.; Baez, E. (2009): Effects of the Rayleigh Number and the Aspect Ratio on 2D Natural Convection Flows. *CMES: Computer Modeling in Engineering & Sciences*, vol. 48, no. 1, pp. 83–105.

Peng, Y.; Shu, C.; Chew, Y. T. (2003): Simplified thermal lattice Boltzmann model for incompressible thermal flows. *Phys. Rev. E*, vol. 68, no. 026701.

Shi, Y.; Zhao, T. S.; Guo, Z. L. (2004): Thermal lattice Bhatnagar-Gross-Krook model for flows with viscous heat dissipation in the incompressible limit. *Phys. Rev. E*, vol. 70, no. 066310.

Su, S. W.; Lai, M. C.; Lin, C. A. (2007): An immersed boundary technique for simulating complex flows with rigid boundary. *Computers & Fluids*, vol. 36, no. 2, pp. 313–324.

Tang, G. H.; Tao, W. Q.; He, Y. L. (2005): Thermal boundary condition for the thermal lattice Boltzmann equation. *Phys. Rev. E*, vol. 72, no. 016703.

Teixeira, C. M. (1998): Incorporating turbulence models into the lattice-Boltzmann method. *International Journal of Modern Physics C*, vol. 9, no. 8, pp. 1159–1175.

Tian, Z. W.; Zuo, C.; Liu, H. J.; Liu, Z. H.; Guo, Z. L.; Zheng, C. G. (2006): Thermal lattice Boltzmann model with viscous heat dissipation in the incompressible limit. *Int. J. Mod. Phys. C*, vol. 17, pp. 1131–1139.

Yang, C. H.; Chang, C.; Lin, C. A. (2009): A Direct Forcing Immersed Boundary Method Based Lattice Boltzmann Method to Simulate Flows with Complex Geometry. *CMC: Computers, Materials & Continua*, vol. 11, no. 3, pp. 209–228.

Yu, D. Z.; Mei, R. W.; Luo, L. S.; Shyy, W. (2003): Viscous flow computations with the method of lattice Boltzmann equation. *Progress in Aerospace Sciences*, vol. 39, no. 5, pp. 329–367.

Appendix A:

Here, the Chapman-Enskog procedure is used to derive the macroscopic energy equation from the thermal lattice Boltzmann equation. The following expansion is similar to that adopted in Deng, Shi, and Wang (2005) for the convection diffusion equation.

Firstly, the multiscale expansion of the temperature distribution function is introduced, i.e.

$$g_i = g_i^{eq} + \varepsilon g_i^{(1)} + \varepsilon^2 g_i^{(2)} + \cdots \tag{34}$$

where ε is the time step $\triangle t$.

Reevaluate Eq. 9 using Eq. 34, the following prevails, i.e.

$$\sum_i g_i^{(k)} = 0, k \geq 1. \tag{35}$$

Applying the multi-scale and Taylor expansions to Eq. 2, the following equation can be obtained,

$$D_i g_i^{eq} + \triangle t D_i g_i^{(1)} + \frac{\triangle t}{2} D_i^2 g_i^{eq} = -\frac{1}{\tau_g}(g_i^{(1)} + \triangle t g_i^{(2)}) + F_i + \frac{\triangle t}{2}\frac{\partial F_i}{\partial t} + O(\triangle t^2) \tag{36}$$

where $D_i = \partial/\partial t + \vec{e}_i \cdot \nabla$ and F_i is,

$$F_i = \omega_i F[1 + \frac{\vec{e}_i \cdot \vec{u}}{C_s^2} \frac{\tau_g - 1/2}{\tau_g}] \tag{37}$$

It is clear that F_i satisfies the following equations.

$$\begin{aligned} \sum_i F_i &= F, \\ \sum_i \vec{e}_i F_i &= ((\tau_g - 0.5)/\tau_g)\vec{u}F \end{aligned} \tag{38}$$

From Eq. 36, we can get the following equation

$$(\triangle t)^0 : D_i g_i^{eq} = -\frac{1}{\tau_g} g_i^{(1)} + F_i + O(\triangle t) \tag{39}$$

Substituting Eq. 39 into the lefthand side of Eq. 36, we can rewrite Eq. 36 as,

$$D_i g_i^{eq} + \triangle t(1 - \frac{1}{2\tau_g})D_i g_i^{(1)} + \frac{\triangle t}{2}\vec{e}_i \cdot \nabla F_i = -\frac{1}{\tau_g}(g_i^{(1)} + \triangle t g_i^{(2)}) + F_i + O(\triangle t^2) \tag{40}$$

Summing Eq. 39 over i and applying Eq. 9, we can obtain

$$\frac{\partial \rho T}{\partial t} + \vec{u} \cdot \nabla \rho T = \sum_i F_i + O(\triangle t) \tag{41}$$

If, F is defined as

$$F = \frac{\Phi}{c_v} \tag{42}$$

and applying Eq. 39 and Eq. 41 to Eq. 40, then we take summation of Eq. 40 over i, we can obtain the macroscopic conservation equation of energy:

$$\frac{\partial T}{\partial t} + \nabla \cdot (\vec{u}T) = \frac{k}{\rho c_v}\nabla^2 T + \frac{\Phi}{\rho c_v} \tag{43}$$

and the thermal conductivity coefficient is determined as $k = \rho c_v C_s^2 \triangle t(\tau_g - 1/2)$.